

Stationary phase approach to the quasiparticle interference on the surface of three dimensional strong topological insulators

Qin Liu *

*State Key Laboratory of Functional Materials for Informatics,
Shanghai Institute of Microsystem and Information Technology, CAS, Shanghai 200050, China*
(Dated: November 13, 2018)

Constant energy contour (CEC) of the surface bands in topological insulators varies not only with materials but also at different energies. The quasiparticle interference caused by scattering-off from defects on the surface of topological insulators is an effective way to reveal the topologies of the CEC and can be probed by scanning tunneling microscopy (STM). Using stationary phase approach, a general analytic formulation of the local density of states as well as the power laws of the Friedel oscillation are present, based only on the time-reversal symmetry and the local geometry around the scattering end points on the CEC. Distinct response of surface states to magnetic impurities from that of nonmagnetic impurities is predicted in particular, which is proposed to be measured in a closed “magnetic wall” setup on the surface of topological insulators.

PACS numbers: 68.37.Ef, 72.25.Dc, 73.50.Bk, 73.20.-r

I. INTRODUCTION

Topological insulators in three dimensions (3D) are band insulators which have bulk insulating gap but gapless surface states with odd number of Dirac cones protected by the time-reversal symmetry (TRS). As an useful surface probe, recent angle-resolved photoemission spectroscopy (ARPES) experiments demonstrate clearly that the bismuth-based class of materials, Bi_2X_3 ($\text{X}=\text{Te}$ or Se), are 3D strong topological insulators (TI) with a single Dirac cone on the surface¹⁻³. The effective surface Hamiltonian when close to the Dirac point is given by $H_0 = \hbar v_F \hat{z} \cdot (\boldsymbol{\sigma} \times \mathbf{k})$, which describes the helical Dirac fermions — charge carriers which behave as massless relativistic particles with spin locked to its momentum. However, compared to the familiar Dirac fermions in particle physics, those emergent quasiparticles from non-trivial surface states of 3DTIs exhibit richer behaviors. In Bi_2Te_3 , an unconventional hexagonal warping effect, $\lambda(k_+^3 + k_-^3)\sigma_z$, appears due to the crystal symmetry⁴, under which the constant energy contour (CEC) of surface band evolves from a convex circle to a concave hexagon as the Fermi surface climbing up away from the Dirac point. This hexagonal warping effect is responsible for the observed snowflake shape Fermi surface¹, being geometrically not as simple as a circle, new interesting phenomena are expected to arise.

Quasiparticle interference (QPI) caused by scattering-off from defects on the surface of 3DTIs is an effective way to reveal the topological nature of the surface states. The interference between incoming and outgoing waves at momenta \mathbf{k}_i and \mathbf{k}_f leads to an amplitude modulation, Friedel oscillation⁵, in the local density of state (LDOS) at wave vector $\mathbf{q} = \mathbf{k}_f - \mathbf{k}_i$. Nowadays, such modulation can be studied by one more powerful sur-

face probe, scanning tunneling microscopy (STM), directly in real space and provide information in momentum space through Fourier transform scanning tunneling spectroscopy (FT-STs). Several STM measurements⁶⁻⁹ with ordinary (spin-unpolarized) tip have been performed on the surface of 3DTIs in the presence of nonmagnetic point and step impurities, and the following features share in common. (i) The topological suppression of backward scattering from nonmagnetic point and edge impurities is confirmed by the observation of strongly damped oscillations in LDOS, accompanied with the invisibility of the corresponding scattering wave vector \mathbf{q} in FT-STs. (ii) Anomalous oscillations are reported in Bi_2Te_3 for both point and edge impurities when the hexagon warping effect starting to work. (iii) Surface bound states exist when near to the point and edge impurities. These experimental facts are theoretically well-explained by different groups¹⁰⁻¹³, however no general analytic expressions of the LDOS have been presented yet. One conclusion in common is now clear that for short-range impurities, different from the well-known R^{-1} and $R^{-1/2}$ power laws of Friedel oscillations in two-dimensional electron gas (2DEG)¹⁴ for point and edge impurities, the leading powers of Friedel oscillations in helical liquid are dominated by the scattering between time-reversal end points (TRP) and are suppressed respectively to R^{-2} and $R^{-3/2}$. This result is the crucial reason of the invisibility of the scattering wave vector \mathbf{q} in FT-STs, and is the direct consequence of the forbiddance of backscattering protected by TRS in helical liquid. Bearing in mind also the reported anomalously pronounced oscillations in LDOS for both point and edge impurities⁶⁻⁹ at bias voltages where the CEC is noncircular but shapes as a snowflake, we become to realize that two ingredients are essential to the oscillations of the LDOS, namely, the TRS of the scattering end points and the geometry of the CEC.

Motivated by these arguments, in this work, we present a general analytic formulation of the LDOS measure-

*E-mail: liuqin@mail.sim.ac.cn

ment in STM experiments using the stationary phase approach.¹⁵ This approach has been taken successfully to study the Ruderman-Kittel-Kasuya-Yosida interaction in 3D systems with nonspherical Fermi surfaces¹⁵, and unusual correlations are obtained. The advantages of this approach reside in that it is sensitive only to the local geometry around the so-called “stationary points” on the CEC, and can be applied not only to bulk states but also to surface states. Using this approach, the followings are obtained. First, a complete result of the power-expansion series of the measured LDOS is tabled for both point- and edge-shaped nonmagnetic and magnetic impurities, modeled by delta potentials, with ordinary and spin-polarized STM tip detection. These results depend only on the TRS and the local geometry around the scattering end points on the CEC at the energy of interest, which explain not only the usual R^{-1} and $R^{-1/2}$ power laws in 2DEG but also the famous R^{-2} and $R^{-3/2}$ oscillations in helical liquid. Second, the most general formulation of the LDOS from CEC beyond the hexagon warping effects is also present, which plays the role of a first-glance guide for future ordinary and spin-polarized STM experiments on potential TI materials with more complicated Fermi surfaces. Furthermore, spin-polarized STM experiments are focused on in particular. It is found that there is no signal for nonmagnetic impurities which is in consistence with the TRS. While for magnetic impurities, pronounced oscillations of LDOS are predicted irrelevant of the TRS of the scattering end points on the CEC, which means the backscattering channels are opened via spin-flip processes¹⁶. A few ARPES experiments with magnetic doping are performed^{16,17}, whereas the spin-polarized STM ones are still lacking and called on. Finally, it is emphasized that our results can also be generalized to surface states of TIs in higher dimensions¹⁸.

We mention that to compare with the recent experiments⁶⁻⁹ in detail, some complexities¹⁰⁻¹³ should still be involved beyond the delta-potential assumption when considering the scattering processes, however this is not the main focus of our work.

The rest of this paper is organized as follows. In Sect. II, we discuss the intuitive picture of the interference between helical waves scattered by magnetic impurities which break the TRS. In Sect. III, we present the general analytic formulation of LDOS for point and edge impurities respectively by focusing firstly on those CEC where the stationary points are extremal points. We then generalize the results to the CEC where the order of the first nonzero expansion coefficient around the stationary points is greater than two. This work is finally concluded in Sect. IV.

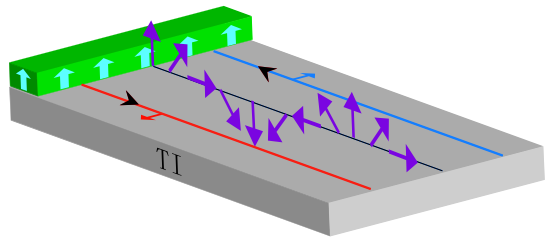


FIG. 1: (Color online) Illustration of charge and spin interferences between two counter-propagating helical waves. The gray block is a 3DTI with a magnetic edge impurity (green stripe) lying in the x -axis on the surface. An incident helical wave along y -axis with spin polarized in the x -direction (blue line) is backscattered by the magnetic edge and the spin is flipped (red line). The interference of the two orthogonal helical waves leads to a constant LDOS in charge channel, but a spiral LDOS in spin channel (purple arrows) in yz -plane.

II. STANDING WAVE OF THE SPIN INTERFERENCE BETWEEN TWO HELICAL WAVES

In the presence of TRS, the backscattering by nonmagnetic impurities on the surface of 3DTIs is known to be forbidden ascribed to the obtained π Berry’s phase during one full rotation of spin^{19,20}. In experiments, this manifests in the invisibility of the scattering vector \mathbf{q} in FT-STs⁹. It would then be interesting to ask how the surface states respond differently to the magnetic impurities, and what is their characteristic signatures in the STM as well as the FT-STs measurements? With magnetic impurities, naively we would expect the interference to be enhanced relative to the nonmagnetic case since the backscattering is restored due to the breaking of TRS. However, it turns out that the charge interference by magnetic impurities is still suppressed as by the nonmagnetic impurities, and there is still lack of notable signals in FT-STs with an ordinary STM tip. The broken TRS would only manifest itself in the spin channel with spin-polarized STM tip²¹.

To understand, we first present a simple picture of the interference between two counter-propagating orthogonal helical waves on the surface of a 3DTI, and then give a theoretical survey in the next section. Suppose there is a magnetic edge impurity placed in the x -axis on the surface, and a helical wave of the surface Hamiltonian H_0 , $\psi_1 = e^{ik_F y} (1 \ i)^T / \sqrt{2}$, where the superscript “T” indicates the transpose, is incident along y -axis with spin locked to x -direction, see Fig.1. This wave is then backscattered by the magnetic edge and counter-propagates in negative y -direction as $\psi_2 = e^{-ik_F y} (1 \ -i)^T / \sqrt{2}$, where its spin is flipped to negative x -direction. A simple calculation shows that the interference between these two counter-propagating helical waves, $\psi = \psi_1 + \psi_2$, leads to a constant charge LDOS on the surface, but a spiral spin LDOS in yz -

FIG. 2: (Color online) Standing wave of spin interference between two helical waves inside a closed “magnetic wall” on top of a 3DTI surface. The out-of-plane spin LDOS is exhibited by the colored rings and the in-plane spin LDOS is indicated by the dark arrows.

plane, $\langle \mathbf{s} \rangle_\psi = [0 \ \sin(2k_F x) \ \cos(2k_F x)]$, where $\mathbf{s} = \sigma/2$ is the electron spin operator. This interference pattern of two orthogonal helical waves in spin channel can be detected by spin-resolved STM experiments. To observe the standing wave of this spin interference pattern, a setup of closed “magnetic wall” as shown in Fig.2 is proposed, where a magnetic layer with a hollow hole is deposited on top of 3DTI surface. Then inside this hole, a standing spin wave is formed with $\langle s_y \rangle \sim \sin(2k_F R)/R^{1/2}$, $\langle s_z \rangle \sim \cos(2k_F R)/R^{1/2}$, and a loop current $j_\phi = -(2\hbar v_F/e)\langle s_z \rangle$ along the azimuthal direction should be observed.

In fact, having in mind the transformation properties under the time-reversal that $\Theta^{-1}\sigma^0\Theta = \sigma^{0T}$, $\Theta^{-1}\sigma^a\Theta = -\sigma^{aT}$, and $\Theta^{-1}G_0(\omega, \mathbf{k})\Theta = G_0^r(\omega, -\mathbf{k})$, where $\Theta = i\sigma_y$ is the time-reversal operator and $a = x, y, z$, it can be proved in the T-matrix formulism immediately that the spin LDOS of nonmagnetic impurities vanishes uniformly and the charge LDOS of magnetic impurities is identical to that of nonmagnetic impurities, by interchanging \mathbf{k} and $-\mathbf{k}'$ in the integrals, see Eq.(1), using $\text{tr}[G_0(\mathbf{k})\sigma^a G_0(\mathbf{k}')\sigma^0] = -\text{tr}[G_0(-\mathbf{k}')\sigma^a G_0(-\mathbf{k})\sigma^0]$. Therefore, in the following, we only need to focus on the response between nonmagnetic impurity and ordinary tip as well as that between magnetic impurity and spin-polarized tip.

III. GENERAL FORMULATION OF STATIONARY PHASE APPROACH TO QPI ON THE SURFACE OF 3DTI

In this section, we formulate a general result of the interference features from quasiparticle scattering on the surface of 3DTIs by nonmagnetic and magnetic impurities with ordinary and spin-polarized tips using the stationary phase approach¹⁵.

A. Point impurity

We start by considering a point defect. The derivation of the LDOS from the constant background measured in STM experiments for a single short-range nonmagnetic or magnetic impurity with ordinary or spin-polarized tip is given by

$$\delta\rho_{\mu\nu}(\omega, \mathbf{R}) = -\frac{1}{\pi}\Im \int \frac{d^2k d^2k'}{(2\pi)^4} e^{i(\mathbf{k}-\mathbf{k}')\cdot\mathbf{R}} \times \text{tr}[G_0^r(\omega, \mathbf{k})T^\mu(\omega, \mathbf{k})G_0^r(\omega, \mathbf{k}')\sigma^\nu]. \quad (1)$$

In the above, $G_0^r(\omega, \mathbf{k})$ is in general the free retarded Green’s function governing the CEC under considera-

tions, and is that of the topological surface band in particular for our interests, where $\mathbf{k} = (k_x, k_y)$. $T^\mu = V/(1 - VG_0^r(\omega))$ is the T-matrix which is \mathbf{k} -dependent for a delta-potential impurity $V(\mathbf{r}) = V\delta(\mathbf{r})\sigma^\mu$, and $G_0^r(\omega) = \int \frac{d^2k}{(2\pi)^2} G_0^r(\omega, \mathbf{k})$. The last Pauli matrix in Eq.(1), σ^ν , represents the polarization of the STM tip, and throughout the paper, we use the Greek index $\mu, \nu = 0$ for nonmagnetic impurity or ordinary tip, and $\mu = a = x, y, z$ for magnetic impurity or spin-polarized tip.

Without loss of generality, we expand the T-matrix to the first order $T^{(1)} = V\sigma^\mu$ and transform the integrand in Eq.(1) to the diagonal basis of the topological surface bands, then the measured LDOS becomes

$$\delta\rho_{\mu\nu}^{(1)}(\omega, \mathbf{R}) = -\frac{V}{\pi}\Im \int \frac{d^2k d^2k'}{(2\pi)^4} e^{i(\mathbf{k}-\mathbf{k}')\cdot\mathbf{R}} \times \sum_{nm} \frac{\Sigma_{nm}^\mu(\mathbf{k}, \mathbf{k}')\Sigma_{nm}^{\nu*}(\mathbf{k}, \mathbf{k}')}{(\omega + i\delta - \varepsilon_n)(\omega + i\delta - \varepsilon'_m)}, \quad (2)$$

where $\varepsilon_{n,m}(\mathbf{k})$ are the spin-splitting bands of the surface states $|n, m\mathbf{k}\rangle$, and we have defined $\Sigma_{nm}^\mu(\mathbf{k}, \mathbf{k}') = \langle n\mathbf{k}|\sigma^\mu|m\mathbf{k}'\rangle$. To calculate the integrals, it is tricky to notice that the contribution to the LDOS along a given direction, say $\mathbf{R} = R\hat{y}$ (here and thereafter we shall always take the y -direction for example), at large distances mainly results in the so-called “stationary points” \mathbf{k}_i ¹⁵, at which

$$\frac{\partial k_y(\varepsilon, t)}{\partial t} = \frac{\partial k'_y(\varepsilon', t')}{\partial t'} = 0, \quad (3)$$

where t and t' are respectively some parameter tangent to the CEC ε and ε' . This is because the phase factors $e^{ik_y(\varepsilon, t)R}$ and $e^{ik'_y(\varepsilon', t')R}$ varies rapidly with respect to t and t' so that most of the integrations cancel out except at the stationary points. This condition singles out the extremal points with nonvanishing second derivatives, such as the pairs connected by \mathbf{q}_1 in a convex CEC in Fig.3 (a) and a concave CEC in Fig.3 (b). Moreover, the condition (3) also allows the turning points such as the pair connected by \mathbf{q}'_2 in Fig.3(b) where the first nonzero derivative being of the third order. In the following, we will focus only on the extremal points for now and leave the general discussions on the others in Sect.III C.

Having identified the pairs of stationary points on the CEC, the integrals in Eq.(2) at large distances are then been approximated by the summation of integrals in the neighborhood of all the stationary point pairs on the CEC. To do this, we first change the integral variables as $d^2k = d\varepsilon dk_x/\hbar|v_{yi}|$ where $v_{yi} = \partial\varepsilon(\mathbf{k})/\hbar\partial k_{yi}$, and then expand the CEC at the extremal points as $k_y = k_{yi} - (k_x - k_{xi})^2/2\rho_{xi}$, where $\rho_{xi} = -[\partial^2 k_y(\varepsilon, k_x)/\partial^2 k_{xi}]^{-1}$ is the principle radii of the curvature of the CEC at the extremal points, which is positive for maxima while negative for minima. Under this approximation, Eq.(2) becomes

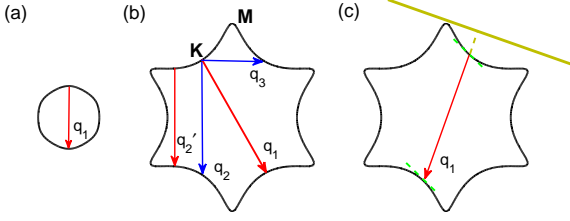


FIG. 3: (Color online) Schematic picture of CEC and stationary points for point and edge impurities. (a) Convex CEC where there is only one pair of stationary points connected by the red arrow along any given direction for both point and line impurities. (b) Concave CEC for point impurity where there are multiple pairs of stationary points. Nonstationary points are shown for example as blue arrows. (c) Concave CEC for edge impurities (brown line) where the slopes (green dashed lines) at the pair of stationary points are the same.

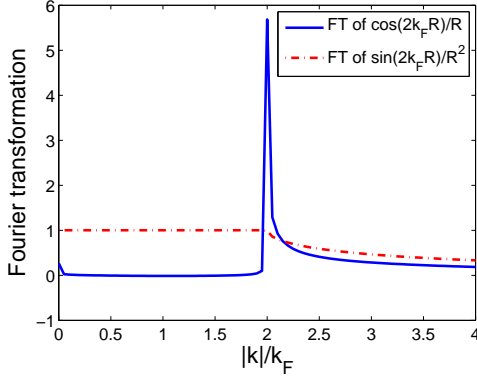


FIG. 4: (Color online) Fourier transformation of the LDOS with R^{-1} and R^{-2} power laws.

$$\begin{aligned}
 \delta\rho_{\mu\nu}^{(1)}(\omega, \mathbf{R}) &\simeq -\frac{V}{\pi} \Im \sum_{mn} \sum_{ij} \int \frac{d\varepsilon_n}{(2\pi)^2} \frac{1}{\omega + i\delta - \varepsilon_n} \frac{e^{ik_{yi}R}}{\hbar|v_{yi}|} \int \frac{d\varepsilon'_m}{(2\pi)^2} \frac{1}{\omega + i\delta - \varepsilon'_m} \frac{e^{-ik'_{yj}R}}{\hbar|v'_{yj}|} \\
 &\times \int_{-\infty}^{\infty} dx e^{-i\frac{x^2}{2\rho_{xi}}R} \int_{-\infty}^{\infty} dx' e^{i\frac{x'^2}{2\rho'_{xj}}R} \Sigma_{nm}^{\mu}(\mathbf{k}, \mathbf{k}') \Sigma_{nm}^{\nu*}(\mathbf{k}, \mathbf{k}'), \tag{4}
 \end{aligned}$$

where $x = k_x - k_{xi}$, $x' = k'_x - k'_{xj}$, and all the quantities at the extremal points (ij) depend still on the energies ε and ε' . The matrix element $\Sigma_{nm}^{\mu}(\mathbf{k}, \mathbf{k}')$ is in general some nonzero constant $C_{ni,mj}^{\mu}(\varepsilon, \varepsilon')$, except when the pair of stationary points are mutually time-reversal symmetric $|n\mathbf{k}_i\rangle = \Theta|m\mathbf{k}'_j\rangle$, which leads to $C_{ni,mj}^0 = 0$ by symmetry. Examples are shown as the

pairs of points connected by \mathbf{q}_1 's in Figs.3(a) and (b) for convex and concave CEC respectively. In such a case, by letting $|n\mathbf{k}\rangle = (e^{i\theta/2} \ e^{-i\theta/2})^{\dagger}/\sqrt{2}$ and $|m\mathbf{k}'\rangle = (e^{i\theta'/2} \ -e^{-i\theta'/2})^{\dagger}/\sqrt{2}$, where $\theta = \arctan(k_y/k_x)$, we expand them around the TRP as $\theta = \theta_i - \alpha$ and $\theta' = \theta'_j + \alpha'$ where $\alpha(\alpha') = x(x')/k_F$, then the matrix elements can be expanded as a series $\Sigma_{nm}^0 = C_{ni,mj}^0 - (x + x')/2k_F +$

$[(x+x')/2k_F]^3/3! + \dots$. Inserting the series into Eq.(4)

and integrating over the energies, we get

$$\delta\rho_{\mu\nu}^{(1)}(\omega, \mathbf{R}) \simeq \frac{V}{2\pi^2\hbar^2 R} \Im \sum_{mn} \sum_{ij} e^{i(k_{yi}-k'_{yj})R} \frac{|\rho_{xi}\rho'_{xj}|^{\frac{1}{2}}}{|v_{yi}v'_{yj}|} \times \left[e^{i(\phi_i-\phi_j)} C_{ni,mj}^\mu C_{ni,mj}^{\omega*} + \frac{1}{4k_F^2 R} \left(e^{i(\phi_i+\phi_j)} |\rho'_{xj}| + e^{-i(\phi_i+\phi_j)} |\rho_{xi}| \right) \right] \Big|_{\varepsilon_F} \quad (5)$$

which is our desired result of the LDOS in STM measurements for point impurity. In the above $\phi_i = -\frac{\pi}{4} \text{sgn}(\rho_{xi})$, and we have used $\int_{-\infty}^{\infty} dx e^{iCx^2} = \sqrt{\pi/|C|} e^{i\frac{\pi}{4} \text{sgn}(C)}$ and $\int_{-\infty}^{\infty} dx x^2 e^{iCx^2} = \sqrt{\pi}/(2|C|^{3/2}) e^{-i\frac{\pi}{4} \text{sgn}(C)}$.

There are several comments regarding this result. First of all, for a pair of non-TRS stationary points like \mathbf{q}_2 in Fig.3(b), the leading power is given by the first term in Eq.(5), which is of R^{-1} . While for a pair of TRS stationary points as \mathbf{q}_1 in Figs.3 (a) and (b), the first nonvanishing contribution to the power law is dominated by the second term in Eq.(5) as R^{-2} for nonmagnetic impurity, and for magnetic impurity but with ordinary tip. This suppression of LDOS is a direct result of the forbiddance of backscattering of helical waves due to TRS. Correspondingly in FT-STs measurements, there is a sharp peak at $2k_F$ for LDOS with R^{-1} power law, which is absent for R^{-2} power law as shown in Fig.4. Interestingly, for magnetic impurities with spin-polarized tip, the first term in Eq.(5) dominates no matter the pair of stationary points is TRS or not, and gives the visibility of the TRS scattering wave vector \mathbf{q}_1 in FT-STs. This distinct response of surface states to magnetic from that of nonmagnetic impurities provides a crucial criteria for the breaking of TRS on the surface of TIs⁶. Second, when integrating over the energies, we have assumed $v_{yi}, v'_{yj} \neq 0$ so that the only poles in the complex energy plane are $\varepsilon = \varepsilon' = \omega + i\delta$. However, in general, it is possible that there are other poles from $v_{yi} = 0$ or $v'_{yj} = 0$, which means the stationary points in CEC are also the extremal points in the energy-momentum dispersion. In such a case, we shall further expand v_{yi} (or v'_{yj}) around ω as $v_{yi}(\varepsilon) = v_{yi}(\omega) + (\partial v_{yi}/\partial \varepsilon)(\varepsilon - \omega) + \dots$, and take the first nonzero term to delete the singularities, whereas this won't modify the power laws. Finally, note that when summation over the stationary point pairs, (ij) , we always choose one in the pair with positive velocity v_{yi} and the other with negative velocity v'_{yj} to obtain the retarded Green's function. Using the general result in Eq.(5), the power laws of LDOS for point impurity are summarized in Table. I according to the classification of TRS of stationary point pairs on the CEC, which can well-explain the recent STM experiments observation in 3DTI.

Before going to the experiments, we first use some concrete examples to illustrate how the formulae of (5)

TABLE I: Power laws from point impurity

		ordinary	spin-polarized
nonmagnetic	TRP	R^{-2}	-
	non-TRP	R^{-1}	-
magnetic	TRP	R^{-2}	R^{-1}
	non-TRP	R^{-1}	R^{-1}

works. The first one is a 2D quadratic CEC, $H_Q = \hbar^2 k^2/2m$, which is isotropic and there are two degenerate spin bands, see Fig.5(a). According to our theory, the main contribution to the LDOS in this example comes from the intraband scattering of the same spin orientation along y -direction between two extremal points, which we denote as '1' for minimum and '2' for maximum. Then at these points explicitly we have $k_{y2} = \rho_{x2} = k_\varepsilon$, $k'_{y1} = \rho'_{x1} = -k_{\varepsilon'}$, $k_\varepsilon = (2m\varepsilon/\hbar^2)^{1/2}$, $v_{y2} = \hbar k_{y2}/m$, $v'_{y1} = \hbar k'_{y1}/m$, and $C_{11}^0 = C_{22}^0 = 1$. Inserting the above into Eq.(5) and keeping only to the leading order, we get $\delta\rho_{00}^{(1)}(\omega, R\hat{y}) \simeq -(Vm^2/\pi^2\hbar^4 k_F) \cos(2k_F R)/R$, which gives R^{-1} power law. Note that the interband contribution whereas to the LDOS is from a pair of TRS extremal points, which has a R^{-2} power law. In contrast, in the example of a 2D Dirac CEC, $H_D = \gamma\sigma \cdot \mathbf{k}$, there is only one non-degenerate band due to the spin splitting, see Fig.5(b). So only intraband scattering between a pair of extremal TRP contributes such that $C_{ni,mj}^0 = 0$, and the leading power is expected to be R^{-2} . Inserting the quantities $k_{y2} = \rho_{x2} = \varepsilon/\gamma$, $k'_{y1} = \rho'_{x1} = -\varepsilon/\gamma$, and $v_{y1(2)} = \gamma \text{sgn}[k_{y1(2)}]/\hbar$ into Eq.(5), we get $\delta\rho_{00}^{(1)}(\omega, R\hat{y}) \simeq (V/4\pi^2\gamma^2) \sin(2k_F R)/R^2$, which is the same as our expectation. In Fig.4, the Fourier transformation of the LDOS for these two examples is shown, where we see that there is a sharp peak at $2k_F$ for LDOS of the 2DEG H_Q , which is greatly broadened in the helical liquid H_D .

In a recent STM measurement of TI, Bi_2Te_3 , with Ag-doped point impurities⁶, clear standing waves and scattering wave vectors are imaged through FT-STs when the Fermi surface is of hexagram shape. It is observed that the high intensity regions are always along the $\bar{\Gamma}$ - \bar{M} direction, but the intensity in $\bar{\Gamma}$ - \bar{K} direction vanishes.

This observation can be well-understood using our stationary phase theory. Among the three wave vectors \mathbf{q}_1 , \mathbf{q}_2 (or \mathbf{q}'_2) and \mathbf{q}_3 with high joint density of states as shown in Fig.3(b), two are connected by the stationary points, namely \mathbf{q}_1 and \mathbf{q}'_2 , while \mathbf{q}_3 (and \mathbf{q}_2) is not. This explains why no standing waves corresponding to \mathbf{q}_3 are observed in FT-STs. Within the other two, stationary points connected by \mathbf{q}_1 are also TRP which shall contribute the power law of R^{-2} according to our result, therefore its intensity in FT-STs is too weak to observe in the experiment along $\bar{\Gamma}-\bar{K}$ direction. For wave vectors \mathbf{q}_2 and \mathbf{q}'_2 along $\bar{\Gamma}-\bar{M}$ direction, \mathbf{q}'_2 is stationary but non-TRS, our result shows that this wave vector has R^{-1} power law, which is responsible for the high intensity reported in Ref.⁶.

B. Edge impurities

Now we turn to the discussion of edge impurity. The edge impurity is assumed to orientate in the x -axis on top of a 3DTI surface, see Fig.1, and be modeled by the Hamiltonian $V(\mathbf{r}) = V\delta(y)\sigma^\mu$. The main difference of the edge impurity from that of the point impurity is the conservation of the momentum along the direction of impurity edge, k_x , which effectively reduces one of the integrations in Eq.(1),

$$\delta\rho_{\mu\nu}(\omega, \mathbf{R}) = -\frac{1}{\pi}\Im \int \frac{d^2k d^2k'}{(2\pi)^4} \delta_{k_x, k'_x} e^{i(\mathbf{k}-\mathbf{k}')\cdot\mathbf{R}}$$

$$\begin{aligned} \delta\rho_{\mu\nu}^{(1)}(\omega, \mathbf{R}) \simeq & -\frac{V}{\pi}\Im \sum_{mn} \sum_{ij} \int \frac{d\varepsilon_n}{(2\pi)^2} \frac{1}{\omega + i\delta - \varepsilon_n} \frac{e^{ik_{yi}R}}{\hbar|v_{yi}|} \int \frac{d\varepsilon'_m}{(2\pi)^2} \frac{1}{\omega + i\delta - \varepsilon'_m} \frac{e^{-ik'_{yj}R}}{\hbar|v'_{yj}|} \\ & \times \int_{-\infty}^{\infty} dx e^{-i\frac{x^2}{2\rho_{xi}}R} \int_{-\infty}^{\infty} dx' e^{i\frac{x'^2}{2\rho'_{xj}}R} e^{i\alpha_{xi}(x-x')} \delta_{x,x'} \left[C_{ni,mj}^\mu C_{ni,mj}^{\nu*} + \frac{(x+x')^2}{4k_F^2} \right]. \end{aligned} \quad (8)$$

Note that though the requirement of momentum conservation, $\alpha_{xi}(x-x') = 0$, makes Eq.(8) the same as that in point impurity case except for a factor $\delta_{x,x'}$, the definition of stationary points are physically quite different

$$\delta\rho_{\mu\nu}^{(1)}(\omega, \mathbf{R}) \simeq \frac{V}{(2\pi)^2\hbar^2} \sqrt{\frac{2}{\pi R}} \Im \sum_{mn} \sum_{ij} \left(\frac{|P_{ij}|^{1/2} e^{i(k_{yi}-k'_{yj})R}}{|v_{yi}v'_{yj}|} \left[C_{ni,mj}^\mu C_{ni,mj}^{\nu*} e^{i\Phi_{ij}} + \frac{|P_{ij}|}{k_F^2 R} e^{-i\Phi_{ij}} \right] \right), \quad (9)$$

where $P_{ij} = \rho_{xi}\rho'_{xj}/(\rho'_{xj}-\rho_{xi})$ and $\Phi_{ij} = -\frac{\pi}{4}\text{sgn}(P_{ij})$. In the above we have assumed $\rho_{xi} \neq \rho'_{xj}$, that is we are not considering the case where the CEC near the pair of sta-

$$\times \text{tr} [G_0^i(\omega, \mathbf{k}) T^\mu(\omega, k_x) G_0^i(\omega, \mathbf{k}') \sigma^\nu] \quad (6)$$

where $T(\omega, k_x) = V(1 - VG_0^r(\omega, k_x))^{-1}$ and $G_0^r(\omega, k_x) = \int \frac{dk_y}{2\pi} G_0^r(\omega, \mathbf{k})$. In the presence of edge impurity, we are usually interested in the LDOS along the direction perpendicular to the impurity edge. Then the main contribution to the LDOS now comes from such pairs of stationary points where their momentum transfer $\mathbf{q} = \mathbf{k}_i - \mathbf{k}'_j$ is normal to the impurity edge and the ‘‘slopes’’ at the pair of points are the same on the CEC,

$$\frac{\partial}{\partial t} [k_y(\varepsilon, t) - k'_y(\varepsilon', t)] = 0. \quad (7)$$

This condition allows more possibilities than those implied by Eq.(3) for point impurity. One such example is shown schematically as \mathbf{q}_1 in Fig.3(c) where the pair of stationary points has the same slope $\alpha_i = \alpha'_j$ (the green dashed lines), with $\alpha_i = \partial k_y(\varepsilon, k_{xi})/\partial k_{xi}$, which is not necessary to be zero. Following the same logic as the discussions in point impurity case in the last subsection, the CEC is expanded around the stationary points as $k_y = k_{yi} + \alpha_i(k_x - k_{xi}) - (k_x - k_{xi})^2/2\rho_{xi}$, and the LDOS is approximated by

and includes more terms in the summation of stationary point pairs (ij) . After integrating out k_x and the energies, it leads to the final result of LDOS in the presence of edge impurity

tionary points is nested, otherwise the quadratic terms in the expansion of CEC cancel out exactly and higher orders expansion should be employed. The power laws of

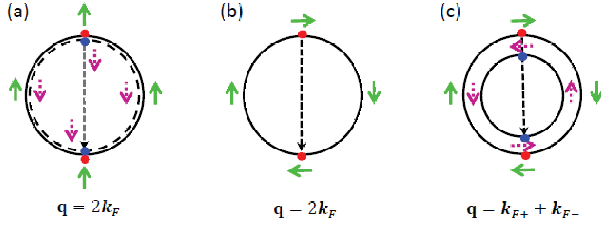


FIG. 5: (Color online) Schematic CEC of (a) quadratic, (b) Dirac, and (c) Rashba dispersions. The spin orientations for each degenerate band are indicated respectively by the green (solid) and purple (dotted) arrows. The stationary points are represented by red and blue dots, which are connected by the scattering vector \mathbf{q} shown as dashed arrows. The intraband scattering comes from the stationary points with the same color, while the interband scattering comes from those with different colors.

LDOS from edge impurity are summarized in Table II, which shall be used to explain the recent STM measurements for edge impurities^{7,8}.

TABLE II: Power laws from edge impurity

		ordinary	spin polarized
nonmagnetic	TRP	$R^{-3/2}$	-
	non-TRP	$R^{-1/2}$	-
magnetic	TRP	$R^{-3/2}$	$R^{-1/2}$
	non-TRP	$R^{-1/2}$	$R^{-1/2}$

To have a feeling of how Eq.(9) works, again we apply it first to the examples of H_Q and H_D used in point impurity. A few lines of calculations yield that for 2D quadratic dispersion, $\delta\rho_{00}^{(1)}(\omega, R\hat{y}) = (Vm^2/2\pi^2\hbar^4k_F^{3/2})\sin(2k_FR - \frac{\pi}{4})/\sqrt{\pi R}$, which recovers the experimental observation in a 2DEG¹⁴. While for 2D Dirac dispersion, $\delta\rho_{00}^{(1)}(\omega, R\hat{y}) = (V/8\pi^2\gamma^2\sqrt{\pi k_F})\sin(2k_FR + \frac{\pi}{4})/R^{3/2}$, which is a result of the absence of backscattering in helical liquid. Similar information in reciprocal space can be extracted via FT-STS as exhibited in Fig.4, where a notable sharp peak appears at $2k_F$ for a 2DEG, which disappears contrastively for helical liquid.

In the recent experiment by Gomes *et al.*, a nonmagnetic step is imaged by STM topography in clean Sb (111) surface with nontrivial topology⁸. The Fermi surface consists of one electron pocket at $\bar{\Gamma}$, which is surrounded by six hole pockets in $\bar{\Gamma}-\bar{M}$ direction, where the surface dispersion shows a Rashba spin splitting. The measured LDOS in $\bar{\Gamma}-\bar{M}$ direction is fitted by a single q -parameter using the zeroth-order of Bessel function of the first kind, see Fig.2(c) in Ref.⁸, which agrees exactly with our prediction in Table. II. Along $\bar{\Gamma}-\bar{M}$ direction, the surface band can be modeled by a Rashba Hamiltonian where the LDOS is dominated by interband scattering between

a pair of non-TRS stationary points, see Fig.5(c). According to our analysis, the Friedel oscillation has $R^{-1/2}$ power law, which is the asymptotic expansion of $J_0(k_FR)$ at large distances. Another STM experiment studies the edge impurity, however in Bi_2Te_2 , is the work by Alpichshev *et al.*⁷, where a nonmagnetic step defect with height about one unit cell is shaped on crystal surface. A strongly damped oscillation is reported when the bias voltage is at the energy with a convex Fermi surface as shown in Fig.3(a). Though no fitting of the experimental data is estimated in this region, our results predict a $R^{-3/2}$ power law. Pronounced oscillations at higher bias voltages where the hexagon warping effect emerges are observed with R^{-1} fitting. Despite of the quantitative difference with our result of $R^{-1/2}$, this R^{-1} oscillations have been explained in several other works^{10,11} beyond our simple model.

Finally, it is emphasized that the results in Tables. I and II provide a quantitative description of the QPI by magnetic impurities in general, and the interference between two orthogonal helical waves as discussed in Sect. II in particular. The interference of helical waves corresponds to the scattering between two TRS stationary points, like the \mathbf{q}_1 's in Figs. 3(a), (b) and (c). The interesting thing is that the LDOS in charge and spin channels from the very same pair of TRS stationary points has quite distinct behaviors. With magnetic impurities, the power laws of charge LDOS are R^{-2} and $R^{-3/2}$ for point and edge impurities respectively, which is a result of TRS and have higher power indices than the R^{-1} and $R^{-1/2}$ modulations of the spin-polarized LDOS, which manifests the TRS breaking. So that the charge LDOS decays much faster than the spin LDOS, and to tell the different response of topological surface states to magnetic impurities from that of the nonmagnetic ones⁶, spin-resolved STM experiments in the proposed closed “magnetic wall” structure in Fig.2 are called on in particular.

C. Friedel oscillations in arbitrarily-shaped CEC

In this section, we shall complete the most general formulation of the QPI on the surface of 3DTI by inclusion those special cases which have been skipped over in the previously discussions.

For point impurity, under the condition (3), we have made the extremal points assumption in Sect. III A that the expansion of CEC around the stationary points has nonvanishing second derivatives. However it is in general possible that ρ_{xi} diverges so that we need to go to the third or even higher order expansions. For example, when the stationary points are also turning points on the CEC. While for edge impurity, under the condition (7), besides the above example of turning points where $\alpha_i = \alpha'_j = \rho_{xi}^{-1} = \rho_{xj}^{-1} = 0$, it is also possible that $\rho_{xi} = \rho'_{xj} \neq 0$ but P_{ij} diverges. This happens when the CEC near the stationary points is nested, and we need to go beyond quadratic term expansions till some power at which the

exact nesting property is unbalanced.

TABLE III: General results of power laws for point impurity

		ordinary	spin-polarized
nonmagnetic	TRP	$R^{-(\frac{1}{l}+\frac{1}{h})-\frac{2}{\min(l,h)}}$	-
	non-TRP	$R^{-(\frac{1}{l}+\frac{1}{h})}$	-
magnetic	TRP	$R^{-(\frac{1}{l}+\frac{1}{h})-\frac{2}{\min(l,h)}}$	$R^{-(\frac{1}{l}+\frac{1}{h})}$
	non-TRP	$R^{-(\frac{1}{l}+\frac{1}{h})}$	$R^{-(\frac{1}{l}+\frac{1}{h})}$

To understand the LDOS behavior in STM experi-

$$\rho_{\mu\nu}^{(1)}(\omega, \mathbf{R}) \propto \frac{V}{R^{\frac{1}{l}+\frac{1}{h}}} \text{Im} \sum_{mn} \sum_{ij} \left\{ \frac{e^{i(k_{yi}-k'_{yj})R}}{|v_{yi}v'_{yj}||\beta_{xi}^{(l)}|^{\frac{1}{l}}|\beta_{xj}^{(h)}|^{\frac{1}{h}}} \left[C_{ni,mj}^{\mu} C_{ni,mj}^{\nu*} + \frac{1}{4k_F^2} \left(\frac{1}{|\beta_{xi}^{(l)}|^{\frac{2}{l}} R^{\frac{2}{l}}} + \frac{1}{|\beta_{xj}^{(h)}|^{\frac{2}{h}} R^{\frac{2}{h}}} \right) \right] \right\}_{\varepsilon_F} \quad (10)$$

$$\rho_{\mu\nu}^{(1)}(\omega, \mathbf{R}) \propto \frac{V}{R^{\frac{1}{\max(l,h)}}} \Im \sum_{mn} \sum_{ij} \left\{ \frac{e^{i(k_{yi}-k'_{yj})R}}{|v_{yi}v'_{yj}||\beta_{xi}^{(l)} - \beta_{xj}^{(h)}|^{\frac{1}{\max(l,h)}}} \left[C_{ni,mj}^{\mu} C_{ni,mj}^{\nu*} + \frac{1}{k_F^2} \frac{1}{(R|\beta_{xi}^{(l)} - \beta_{xj}^{(h)}|)^{\frac{2}{\max(l,h)}}} \right] \right\}_{\varepsilon_F} \quad (11)$$

where the notations $\min(l, h)$ and $\max(l, h)$ represent taking the minimum or the maximum one in-between l and h . The corresponding power laws of LDOS are listed in Tables. III and IV. We see that by setting $l = h = 2$,

TABLE IV: General results of power laws for edge impurity

		ordinary	spin-polarized
nonmagnetic	TRP	$R^{-\frac{3}{\max(l,h)}}$	-
	non-TRP	$R^{-\frac{1}{\max(l,h)}}$	-
magnetic	TRP	$R^{-\frac{3}{\max(l,h)}}$	$R^{-\frac{1}{\max(l,h)}}$
	non-TRP	$R^{-\frac{1}{\max(l,h)}}$	$R^{-\frac{1}{\max(l,h)}}$

Tables. I and II are recovered. Eqs. (10) and (11) in principle can be used to describe the QPI on an arbitrarily-shaped CEC, which is very useful as a first-glance guide of the freshly cooked experimental data.

IV. CONCLUSIONS

In conclusion, general analytic expressions of the LDOS are derived in Eqs.(5), (9), (10), and (11) us-

ments in these situations, we assume that the first non-vanishing terms in the expansions of k_y and k'_y around the stationary points are in general respectively $k_y = k_{yi} + \beta_i^{(l)}(k_x - k_{xi})^l$ and $k'_y = k'_{yj} + \beta_j^{(h)}(k'_x - k'_{xj})^h$, where $l, h \in \mathbb{Z}$ and the β 's are the expansion coefficients which is explicitly $\beta_i^{(l)} = (\partial^l k_y / \partial k_{xi}^l) / l!$ and similar for $\beta_j^{(h)}$. Notice that for edge impurity, if $l = h$ one more constrain $\beta_i^{(l)} \neq \beta_j^{(h)}$ is further required in particular. Then similar calculations as performed in Sects. III A and III B lead to the following results for point and edge impurities separately, that

ing the stationary phase approach, for nonmagnetic and magnetic point and edge impurities in ordinary and spin-polarized STM experiments. The power laws of Friedel oscillation are extracted in Tables. I to IV in particular. The QPI from magnetic impurities are focused on, in which the interference of charge intensity is indistinguishable from that of nonmagnetic impurities, while the spin intensity of magnetic impurities shows distinctive FTSTS patterns, which is proposed to be realized in a closed ‘‘magnetic wall’’ setup through spin-polarized STM measurements. Our results depend only on the TRS as well as the local geometry around the stationary points on the CEC, so that they are suitable especially as a first-glance guide of the experiments with ever changing Fermi surfaces, like the emergence of the hexagon warping effects in Bi_2Te_3 .

Acknowledgments

The author would like to thank Xiao-Liang Qi and Shou-Cheng Zhang for illuminating discussions. This work is supported by the NSFC (Grant Nos. 11004212, 10704080, 60877067, and 60938004) and the STCSM (Grant Nos. 08dj1400303 and 11ZR1443800).

¹ Y.L. Chen *et al.*, Science **325**, 178 (2009).

² Y. Xia *et al.*, Nat Phys. **5**, 398 (2009).

³ D. Hsieh *et al.*, Nature (London) **460**, 1101 (2009).

⁴ L. Fu, Phys. Rev. Letts. **103**, 266801 (2009).

- ⁵ J. Friedel, *Phil. Mag.* **43**, 153 (1952).
- ⁶ Tong Zhang *et al.*, *Phys. Rev. Lett.* **103**, 266803 (2009).
- ⁷ Zhanybek Alpichshev *et al.*, *Phys. Rev. Lett.* **104**, 016401 (2010).
- ⁸ Kenjiro K. Gomes *et al.*, arXiv:cond-mat/0909.0921 (unpublished).
- ⁹ Pedram Roushan *et al.*, *Nature* **460**, 1106 (2009).
- ¹⁰ X. Zhou, C. Fang, W.-F. Tsai, and J.P. Hu, *Phys. Rev. B* **80**, 245317 (2009).
- ¹¹ W.-C. Lee, C. Wu, D. P. Arovas, and S.-C. Zhang, *Phys. Rev. B* **80**, 245439 (2009).
- ¹² H.-M. Guo, and M. Franz, *Phys. Rev. B* **81**, 041102(R) (2010).
- ¹³ Rudro R. Biswas, and Alexander V. Balatsky, e-print arXiv:1005.4780 (unpublished); *Phys. Rev. B* **81**, 233405 (2010), **83**, 075439 (2011).
- ¹⁴ M. F. Crommie, C. P. Lutz, and D. M. Elgler, *Nature (London)* **363**, 524 (1993).
- ¹⁵ Laura M. Roth, *Physical Review* **149**, 519 (1966).
- ¹⁶ Z.-H. Pan *et al.*, e-print arXiv:1104.0966.
- ¹⁷ Y. L. Chen *et al.*, *Science* **329**, 659 (2010).
- ¹⁸ X.-L. Qi, T.L. Hughes, and S.-C. Zhang, *Phys. Rev. B* **78**, 195424 (2008).
- ¹⁹ Tsuneya Ando, Takeshi Nakanishi, and Riichiro Saito, *J. Phys. Soc. Japan* **67**, 2857 (1998).
- ²⁰ X.-L. Qi and S.-C. Zhang, *Phys. Today* **63**, 33 (2010).
- ²¹ Q. Liu, C.-X. Liu, C. Xu, X.-L. Qi, and S.-C. Zhang, *Phys. Rev. Lett.* **102**, 156603 (2009).